Carbon 98 (2016) 58–66

Contents lists available at ScienceDirect

Carbon

journal homepage: www.elsevier.com/locate/carbon

Tube-like carbon for Li-ion capacitors derived from the environmentally undesirable plant: *Prosopis juliflora*

Palanichamy Sennu [a], Hyun-Jun Choi [a], Seul-Gi Baek [a], Vanchiappan Aravindan [b, *], Yun-Sung Lee [a, **]

[a] Faculty of Applied Chemical Engineering, Chonnam National University, Gwang-ju, 500-757, Republic of Korea
[b] Energy Research Institute @ NTU (ERI@N), Nanyang Technological University, Research Techno Plaza, 50 Nanyang Drive, Singapore, 637553

ARTICLE INFO

Article history:
Received 19 June 2015
Received in revised form
26 October 2015
Accepted 28 October 2015
Available online 31 October 2015

ABSTRACT

This work describes the fabrication of high-energy Li-ion hybrid electrochemical capacitors (Li-HEC) from the environmentally threatening and invasive *Prosopis juliflora*. The carbon derived from this acts as the positive electrode active material in organic medium. High-surface-area carbon was obtained from *P. juliflora* and activated using KOH at various concentrations and temperatures. Of the tested ratios, 1:2 (carbon: KOH) treated at 900 °C (KC21-900) yielded a high specific surface area (2410 $m^2\ g^{-1}$) and specific capacitance (~161 F g^{-1}). Then, a Li-HEC was fabricated with a homemade insertion-type $Li_4Ti_5O_{12}$ negative electrode, delivering a maximum energy density of ~80 W h kg^{-1}. In addition, the prepared Li-HEC had excellent cycleability (10000 cycles) and good capacity retention characteristics.

1. Introduction

Sustainable renewable energy generation from sources that would otherwise be environmental pollutants and transportation of such energies for the desired applications would lead to significant global social and economic development. The principle disadvantage of commercially available energy storage devices such as supercapacitors and Li-ion batteries (LIB) is that they have low roundtrip efficiencies and poor power capabilities. Moreover, their energy and power densities are significantly lower than those necessary for applications in zero-emission transportation such as electric vehicles (EV, >150 W h kg^{-1}) and plug-in hybrid electric vehicles (P-HEV, 57 to 97 W h kg^{-1}) [1]. Among the electric storage devices, Li-ion batteries are capable of delivering the necessary energy density, but the power capability is not sufficient for use in vehicles. Nevertheless, supercapacitors, preferably electric double layer capacitors (EDLC), are capable of having high power capabilities, but have lower energy densities. Therefore, an electrochemical energy storage device that is capable of delivering high energies and power densities is required to fulfill the power requirements of these vehicles [2–4]. More specifically, the new storage device must fill the gap between rechargeable batteries and conventional supercapacitors. Amatucci et al. [5–7] first introduced the concept of hybridizing high energy LIB and high power EDLC's in aprotic organic media to achieve a high energy density without compromising the high power capability. Generally, this new electrochemical energy storage device, i.e., Li-ion hybrid electrochemical capacitor (Li-HEC), is constructed with a Li-ion insertion type battery component (LIB electrode) and a double-layer forming supercapacitor component as the counter electrode, which provides the desired energy and power densities, respectively. For the battery component, numerous Li-ion insertion type electrodes have been investigated for Li-HEC applications. $Li_4Ti_5O_{12}$ remains the most popular for various reasons, and it has been clearly described in our recent reviews [2,8]. However, there are few reports about the supercapacitor component [9–14]. Carbonaceous material is the unanimous choice for the supercapacitor electrodes, i.e., activated carbon (AC), due to its high electrical conductivity, tailored morphology, high specific surface area, and eco-friendliness. The choice of carbon precursor and activation conditions determine the electrochemical performance of such materials via surface area, pore-size distribution, electrical conductivity and the presence of electrochemically active surface functional groups [15,16]. Recent research has shown that high-surface-area carbonaceous material derived from biomass, such as seaweed biopolymers, waste coffee beans, corn grains, banana fibers, pinecones, etc., have notable

* Corresponding author.
** Corresponding author.
E-mail addresses: aravind_van@yahoo.com (V. Aravindan), leeys@chonnam.ac.kr (Y.-S. Lee).

http://dx.doi.org/10.1016/j.carbon.2015.10.087
0008-6223/

supercapacitive properties [17–19]. *Prosopis juliflora* is an environmentally threatening, invasive weed and has invaded millions of hectares of land in the arid and semi-arid areas of Asia, Africa, Australia, and America. The tree absorbs atmospheric humidity and, thus, reduces rainfall. In addition, its growth has displaced native flora and fauna. Therefore, many countries are attempting to remove *P. juliflora* permanently, the so-called '*juliflora* abolish movement'. However, the wood is dimensionally stable and has good mechanical properties. In addition, it is used predominantly as wood fuel, in construction sites, and it could be a valuable alternative to remedy wood shortage that would reduce pressure on natural and plantation forests. Bearing this in mind, we attempt to use this material for energy storage applications, particularly, the development of a high energy Li-HEC. Prior to testing the *P. juliflora* AC as an electrode for charge storage, we have carried out a systematic study on the preparation of AC from *P. juliflora*. Firstly, the influence of the pore forming agent, i.e., KOH, and its capacitive behavior has been evaluated in symmetric configuration. Subsequently, the energy density has been increased by introducing a homemade insertion type electrode $Li_4Ti_5O_{12}$ with *P. juliflora* derived AC as the supercapacitor component in a Li-HEC assembly. In addition, extensive physico-chemical properties, including XRD, BET surface area, Raman analysis, XPS, and SEM studies, were conducted and are described in detail.

2. Experimental section

2.1. Preparation of AC and $Li_4Ti_5O_{12}$

P. juliflora wood (Karuvelam-KV-Cs) was used as the starting material. The dried *P. juliflora* wood was washed with water and dried at 60 °C for 24 h and cut into small pieces. The small pieces were charred at 250 °C for 1 h. Then the black colored char was ground into a fine powder and treated with different weight ratios of KOH at 120 °C for 3 h. Then, the mixture was activated at 800 and 900 °C under an N_2 flow at a heating rate of 5 °C min^{-1} for 3 h. After cooling to room temperature, the resultant product was washed thoroughly several times with de-ionized water until the pH value became neutral. The washed powder was under vacuum dried and used for various characterization studies. KV-Cs obtained at 800 °C with KOH: Carbon weight ratios of 0:1, 1:1, and 2:1 are designated KC01-800, KC11-800, and KC21-800, respectively. At 900 °C, only the 1:2 ratios KOH was tested and is designated KC21-900.

Insertion type, $Li_4Ti_5O_{12}$ (BET specific surface area: 3.73 ± 0.35 m^2 g^{-1}) was synthesized by solid state reaction. In the typical process, stoichiometric amounts of $LiOH \cdot H_2O$ (Junsei, Japan) and TiO_2 (anatase form, Junsei, Japan) were used. The mixture was finely ground and pre-calcined at 400 °C for 10 h and calcined at 800 °C for 20 h in an O_2 atmosphere using a tubular furnace to yield the desired phase.

2.2. Physical characterizations

The crystalline phase of the resulting material was studied by powder X-ray diffraction (XRD, Rint 1000, Rigaku, Japan) using CuK_α radiation. BET surface area measurements were performed by using a Micromeritics ASAP 2010 surface area analyzer. Morphological features of the samples were recorded by using a scanning electron microscope (FE-SEM, S4700, Hitachi, Japan). X-ray photoelectron spectroscopy (XPS) was also performed using a Multilab 2000, (Thermo Scientific, UK) with monochromator and Al$K\alpha$ radiation ($h\nu$ = 1486.6 eV).

2.3. Electrochemical characterization

All the electrochemical measurements were performed in standard CR2032 coin-cell configuration. The composite electrodes were formulated with accurately weighed amounts of the active materials (80% or 8 mg), ketzen black (10% or 1 mg), and teflonized acetylene black (10% or 1 mg, TAB-2) slurried with ethanol. The slurry was pressed over a stainless-steel mesh (16 mm diameter, 200 mm^2 area) and dried at 160 °C for 4 h in a vacuum oven. The symmetric and Li-HEC assemblies were constructed in two electrode configuration, separated by a porous polypropylene (Celgard 3401, USA) film and filled with 1 M $LiPF_6$ in ethylene carbonate (EC)/di-methyl carbonate (DMC) (1:1 v/v, Soulbrain Co. Ltd, Korea). Cyclic voltammetry (CV) and electrochemical impedance spectroscopy (EIS) studies were performed using an electrochemical work station (Bio-Logic (SP-150), France). Galvanostatic charge–discharge studies were performed at different current densities using a conventional battery tester (WBCS 3000, Won-A-Tech, Korea) under ambient conditions. The electrochemical parameters were calculated using formulas described elsewhere [11,14,20,21]. The corresponding specific capacitance was calculated from the following equation,$C = 4I \times \Delta t/m \times \Delta V$, where C is the specific capacitance (Fig. 1), I is applied current (A), Δt represents discharge time (s), ΔV represents the potential window (V), and m is the total mass of the electrodes (g). Specific energy (E) and power densities (P) are calculated using following relations: $P = (\Delta E \cdot i/m)$ and$E = (P \cdot t)$, where $\Delta E = (E_{max} + E_{min})/2$ and E_{max} and E_{min} are respectively the potential at beginning of discharge and at the end of discharge curves of galvanostatic cycle.

3. Results and discussion

3.1. Physico-chemical properties

Fig. 1 shows the XRD pattern and BET specific surface area of KV-C's and insertion type $Li_4Ti_5O_{12}$ (LTO). As shown in Fig. 1a, all KV-C's have similar diffraction patterns without any sharp reflections, corresponding with the amorphous nature of the carbon derived from *P. juliflora*. The intensity of the broad reflection located at 2θ = ~25° (d_{002}) for KV-C10-800 decreased upon activation with KOH, irrespective of the KOH concentration and sintering temperature. Nevertheless, a notable improvement in crystallographic ordering is observed from the calculation of $d100/d_{002}$ ratio, indicating an increase in the degree of graphitization [12]. The microstructure and crystallinity of LTO is shown in Fig. 1b. The most intense diffraction peaks of the pristine sample at 18.4°, 43.3°, and 62.9° correspond to the (111), (004) and (044) reflections of the standard LTO phase (space group: $Fd\bar{3}m$, ICSD card no. 98-001-5787), respectively. A phase pure LTO could be obtained without any impurity traces such as Li_2TiO_3 and rutile TiO_2. The N_2 adsorption–desorption isotherms for KV-Cs activated with various amounts of KOH at different temperature and LTO are shown in Fig. 1c. At low-pressure conditions, rapid increases in adsorption–desorption isotherms are evident, which is consistent with the IUPAC classification for type-I isotherm (Fig. 1c). The major uptake occurs at low relative pressures, indicating activated carbons with microporous structure with narrow pore size distribution (Fig. S1). The effect of temperature during activation on the BET surface area and pore volumes (total, micropore, and mesopore) of the KV-Cs and LTO are shown in Table 1. The specific surface area and pore volume of the KV-Cs were gradually increased with KOH concentration (from 1:0 to 1:2 ratios) and carbonization temperatures (from 800 to 900 °C). The specific surface area for KC21-900 and LTO were found to be 2410 and 3.7376 m^2 g^{-1} and total pore volumes were 1.1963 and 0.020913 cm^3 g^{-1}, respectively. The micro

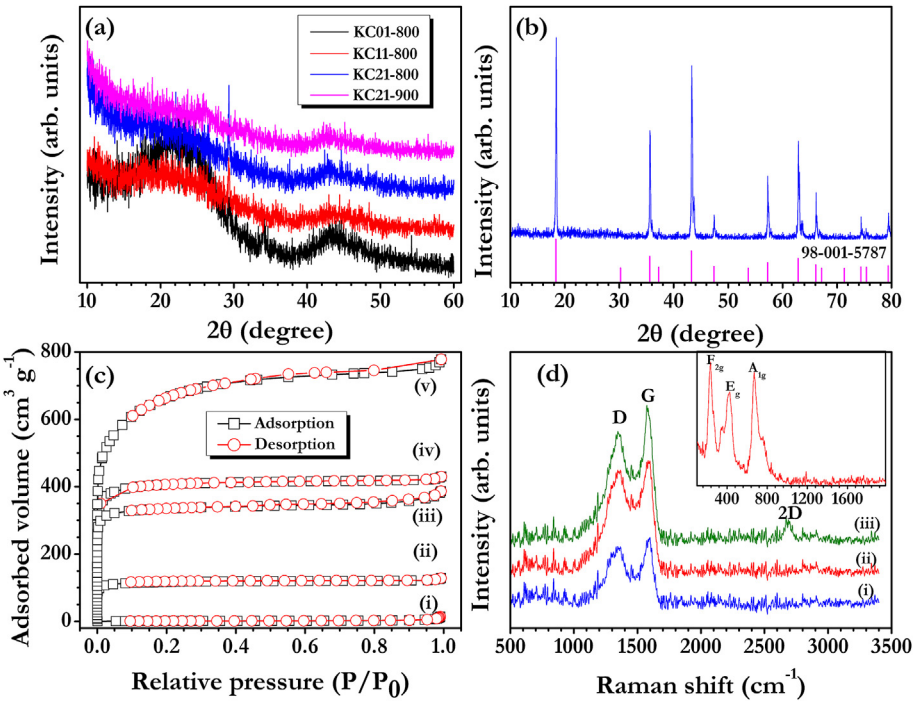

Fig. 1. XRD patterns of (a) activated KV carbons derived from *P. juliflora* and (b) $Li_4Ti_5O_{12}$ (LTO), (c) N_2 adsorption/desorption isotherms of (i) LTO, (ii) KC01-800, (iii) KC11-800, (iv) KC21-800, and (v) KC21-900, (d) Raman spectra of (i) KC11-800, (ii) KC21-800, and (iii) KC21-900. (A color version of this figure can be viewed online.)

Table 1
BET surface area, total pore volume, and average pore diameter of different biomass activated carbon from KC01-800, KC11-800, KC21-800, and KC21-900.

Sample	S_{BET}[a] ($m^2\ g^{-1}$)	V_{total}[b] ($cm^3\ g^{-1}$)	V_{micro}[c] ($cm^3\ g^{-1}$)	V_{meso}[d] ($cm^3\ g^{-1}$)	Average pore diameter (nm)
KC01–800	455 ± 19	0.1964	0.1800	0.0164	1.7251
KC11–800	1334 ± 29	0.5922	0.4915	0.1007	1.7757
KC21–800	1589 ± 34	0.6624	0.6327	0.0297	1.6672
KC21–900	2410 ± 48	1.1963	1.1202	0.0761	1.9854

[a] S_{BET} is the BET surface area and it was measured at relative pressure of 0.990.
[b] Total pore volume (V_{total}) was the single point adsorption total pore volume of pores less than 400 nm diameter at $P/P_0 = 0.990$.
[c] V_{micro} is the micro pore volume.
[d] V_{meso} is the meso pore volume.

and meso-porosities also changed with the activation temperature and KOH concentration. Raman spectroscopy is one of the important tools for studying carbonaceous materials, particularly for the nature of carbon and degree of graphitization during the activation process. Fig. 1d represents the Raman spectra of KC11-800, KC21-800, KC21-900, and LTO. In the case of KV-Cs, G and D bands were positioned at ~1580 and ~1345 cm^{-1}, respectively [22,23]. The ratio between the intensities of D and G bands (I_D/I_G) was used to predict the degree of graphitization and formation of defects by lattice distortion within the samples [24]. The intensity I_D/I_G ratios of KC11-800 (0.91) and *KC21-800* (0.93) were almost equal, suggesting the presence of defects only at low temperature. Further, with increased activation temperature (KC21-900), a decrease in I_D/I_G ratio (0.87) and shifting of G band towards the lower wave number (~1584–~1573 cm^{-1}) were observed, which signifies the increase in electrical conductivity [9]. The KC21-900 exhibits the G band at ~1573 cm^{-1} owing to the Raman-active E_{2g} mode, which is analogous to that of graphite, whereas the reflections at ~1346 cm^{-1} (D-band) and ~2683 cm^{-1} (2D-band) mainly originated from the defects [22,23,25]. Raman spectrum of LTO confirmed the formation of a cubic spinel structure and composed of three predominant reflections at ~235, ~425, and ~671 cm^{-1} that are associated with the F_{2g}, Eg, and A_{1g} vibration modes of O–Ti–O bond, Li–O bond in LiO_4, and LiO_6 polyhedral, and Ti–O bond in TiO_6 octahedral environment, respectively.

SEM pictures of AC derived from biomass (selected samples) and spinel phase LTO are shown in Fig. 2. Fig. 2a depicts the carbon treated at 800 °C for 3 h in N_2 atmosphere without any activating agent. The AC showed a tubular structure derived from *P. juliflora* wood, and few macro pores were also created by the partial evaporation of cellulose type materials. Cracking and agglomeration occurred on the char in a high temperature sintering process. The external surface of the KOH-treated carbon is shown in Fig. 2b and c. Both, KC21-800 and KC21-900 exhibited pores, which were formed on the surfaces and inside the cavities. It is apparent that the pore and cavity formation resulted from the charring of cellulose with KOH [26,27]. Spaces were eventually between the core and an edge site of the carbons by gasification at high-temperature activation (preferably CO and CO_2). The percentage of pore formation in carbonaceous material depends entirely on the weight ratio of the KOH incorporated upon activation. The surface structure of KV carbons activated with 1:2 (carbon: KOH) ratio is shown in Fig. 2b and c. Increases in sintering temperature from 800 to 900 °C created more pores by gasification, which eventually affected the interior and exterior surfaces of carbon. The cracked and flake type surface morphology was observed for such high KOH loading

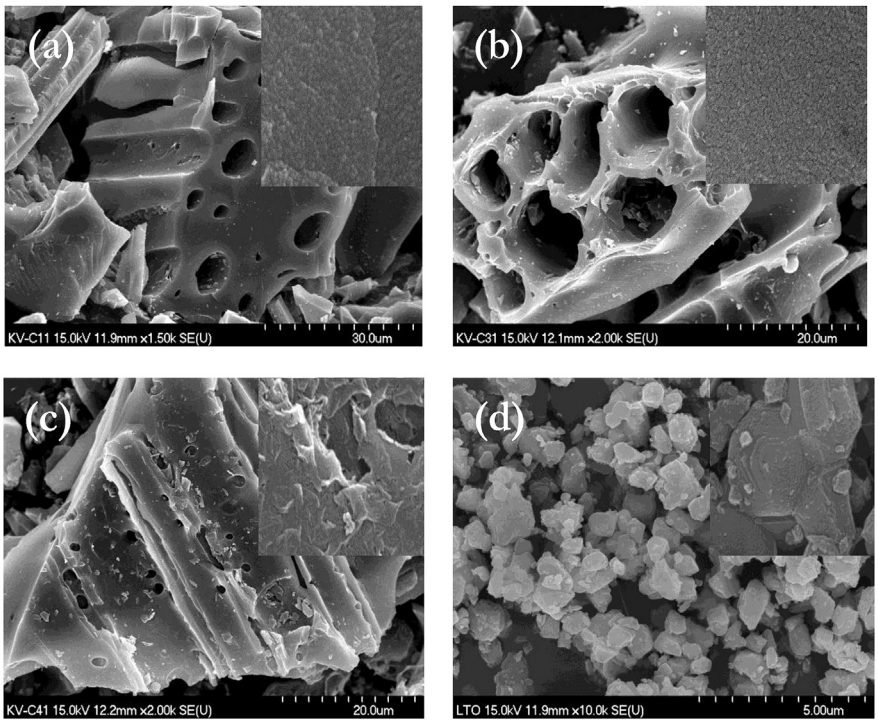

Fig. 2. SEM images of (a) KC01-800, (b) KC21-800, and (c) KC21-900; Biomass carbons naturally exist in a tubular structure. (d) LTO nanoparticle, which exist as nanoflakes (inset).

(KC21-800 and KC21-900). In addition, the presence of Ca during pore formation cannot ascertain because Ca is a well-known activating agent. The carbonization temperatures for chemical activation to increase the pore volume and BET surface area are confirmed from Table 1. As expected, increases in KOH concentration and temperature resulted in the increase in specific BET surface area. An SEM picture of LTO particles prepared by solid-state approach revealed an average particle size of 1–3 μm in diameter. The LTO particles are homogenous in size and shape with a flake-like morphology.

Surface features of the AC derived from *P. juliflora* wood were further explored by X-ray photoelectron spectroscopy (XPS) and given in Fig. 3, S2, and S3. Fig. 3a shows the survey spectrum of KC21-900, and features different elements such as O, Ca, S, and N with ~21.86,~3.5, ~1.11, and ~0.86 at.%, respectively. This implies that there are abundant carbons functionalities present in KC21-900. The high-resolution de-convoluted C 1s spectrum is shown in Fig. 3b. The core-level spectra of C 1s confirm the well resolved peaks corresponding to carbon atoms in different chemical environments, for example, binding energies at ~284.58 (sp^2 graphitic C), ~285.43 (sp^3 graphitic C), ~286.7 (C–N or C–O), ~288.6 (C=O), and ~291.39 eV ($\pi-\pi^*$) [28–30]. The *sp3* bond configuration forms $\sigma-\sigma^*$ bands and the sp^2 sites create $\pi-\pi^*$ bands by forming the localized density of states. The mass percentages of the sp2 cluster (32.38%) dominate the electrical properties of carbon. The O 1s spectrum (Fig. 3c) exhibited three resolved peaks at ~531.85, ~532.84, and ~534.87 eV, suggesting that the oxygen bonded with different compound groups, such as C–O, C=O, and O–S [29–31]. Fig. 3d represents the Ca 2p [32] spectrum and features two main peaks at ~347.82 eV for Ca $2p_{3/2}$ and ~351.45 eV for Ca $2p_{1/2}$. The spin–orbit splitting between these two peaks are at ~3.63 eV, which confirmed that the Ca 2p existed in Ca–O or Ca–CO_x compositions. The N 1s and S 2p spectrum are also shown in Fig. S3; the peaks at ~400.07 and ~168.8 eV originated from C–NH_2 and M–SO [31,33], respectively.

3.2. Symmetric supercapacitor

Symmetric supercapacitors were fabricated in the presence of an organic medium using *P. juliflora* derived carbons as the electrode. Carbons with a high specific surface area are one of the prerequisite for the utilization of electrodes in supercapacitor fabrication, irrespective of aqueous or organic mediums. Fig. 4a shows the electrochemical performance of KC01-800, KC11-800, KC21-800, and KC21-900 in a symmetric configuration between 0 and 3 V at a scan rate of 5 mV s^{-1}. The observed CV traces clearly exhibited a rectangular curve without any redox peaks, which is a typical characteristic of EDLC behavior of carbonaceous material. The shape and area of KC21-900 CV curve was much better and higher than the rest of the electrodes tested. The rectangular shape was preserved for KC21-900, even the scan rate was increased to 50 mV s^{-1} (Fig. S4). This results mainly in larger micro- and mesopore volumes, apart from the high specific surface area. The larger pore-volume certainly enables the facile adsorption/desorption of PF_6^- anions and subsequently leads to the double layer formation across the electrode/electrolyte interface. The high surface area provides more active sites for the electric double layer formation. Overall, KC21-900 proved to have good charge propagation by the adsorption/desorption of ions without any pseudocapacitive tendencies. Based on the above performance, in-depth electrochemical investigations were conducted only for KC21-900. Accordingly, CV studies were conducted at various sweep rates (5, 10, and 50 mV s^{-1}) to ensure the EDLC behavior (Fig. 4b). At high scan rates, CV traces slightly deviated from their ideal rectangular shape, which was common for all the materials. This behavior was mainly because of the low ionic mobility and less active material participation upon electrochemical reaction. However, in the present work, until 50 mV s^{-1} the pattern of CV curves remained in a symmetrical rectangular shape, which indicated the high power capability of KC21-900. During electrochemical reactions, the ion-buffering reservoirs in the macropores were easily transferred to

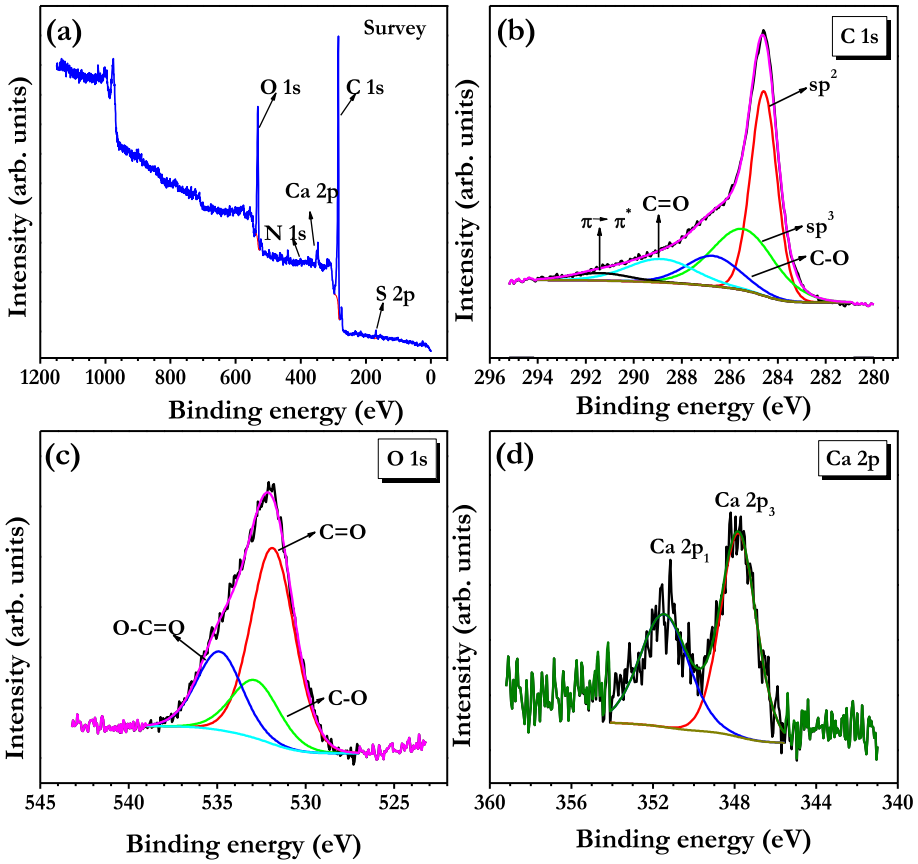

Fig. 3. (a) XPS survey spectrum of *Prosopis juliflora* derived from KC21-900 carbon. Different elements occur naturally and their core level spectra are given in (b) C 1s, (c) O 1s, and (d) Ca 2p. (A color version of this figure can be viewed online.)

the interior surfaces of carbon towards the double layer formation. Further, presence of mesopore walls certainly provided a less-resistant pathway for ion transport and eventually strengthened the electric double layer formation. The different porous nature of KC21-900 helped in maintaining a good capacitive behavior at high current rates, and further in shortening the diffusion pathway between mesopores and microspores, which certainly enhanced facile ionic transportation. In addition, the optimum level of oxygen functionalities binding with Li based on the enolization process, which also contributed to capacitance and stability upon cycling [34]. Galvanostatic charge–discharge performance and cycleability of the KC21-900 based symmetric supercapacitor were tested at 1 A g^{-1} and are shown in Fig. 4c. Here, the applied current density was calculated based on the total mass of the electrodes. It can be found that the KC21-900 exhibited a higher specific capacitance (~140 F g^{-1}) compared to KC21-800 (~80 F g^{-1}). The triangular smooth charge–discharge patterns were consistent with the above CV results. Upon cycling, ~91% of initial capacitance was retained for KC21-900, whereas only 47% of retention was noted for KC21-800 after 5000 cycles (Fig. S5). These results indicated that the KC21-900 not only showed excellent EDLC behavior but also excellent cycling stability.

The charge–discharge profile for KC21-900 at various current densities is presented in Fig. 5a. The maximum specific capacitance of ~161 F g^{-1} was achieved at a current density of 0.1 A g^{-1}. Even at a current density of 2 A g^{-1}, a specific capacitance of 125 F g^{-1} was noted. The specific capacitance as a function of current densities is shown in Fig. 5b. From the above results, it is apparent that the KC21-900 showed attractive performances in symmetric configuration with high specific capacitance and long life cycle.

3.3. Li-ion hybrid electrochemical capacitor (Li-HEC)

Generally, low energy density is one of the prime issues of symmetric supercapacitors irrespective of aqueous or organic mediums [35,36]. The utilization of organic mediums certainly enhances energy density, but it is not sufficient to drive the EV and HEV. Therefore, a dramatic improvement in the energy density is required without compromising the high power capability. Introducing insertion type electrodes for the fabrication of Li-HEC is one of the efficient approaches to improve energy density. In this regard, insertion type (LTO) was introduced as a negative electrode along with KC21-900 as a positive terminal for the construction of a Li-HEC in the presence of 1 M $LiPF_6$ in EC:DMC solution. Before constructing the Li-HEC, mass loading has to be balanced between the charges at positive (q_+) and negative (q-) electrodes [37]. Therefore, single electrode performances of both electrodes were analyzed with metallic Li under the same current density (0.1 A g^{-1}) for the optimization process (Fig. S6 and Fig. S7). Accordingly, based on specific capacity of individual electrodes, Li-HECs were fabricated by adjusting the optimal mass ratio between negative (4 mg) and positive (9 mg) electrodes (1:2.25, $m_{LTO}/m_{KC21\text{-}900} = 0.44$).

Prior to this, performances of KC01-800, KC11-800, and KC21-800 electrodes were also evaluated and compared with KC21-900 under similar testing conditions (Fig. S6). As expected, a high reversible capacity (~80 mAh g^{-1}) was noted for KC21-900 with good cycling characteristics irrespective of the applied current densities. Fig. S7a clearly shows linear variations of charge–discharge curves with respect to time. This clearly showed the perfect double layer formation with PF_6^- anion and is well

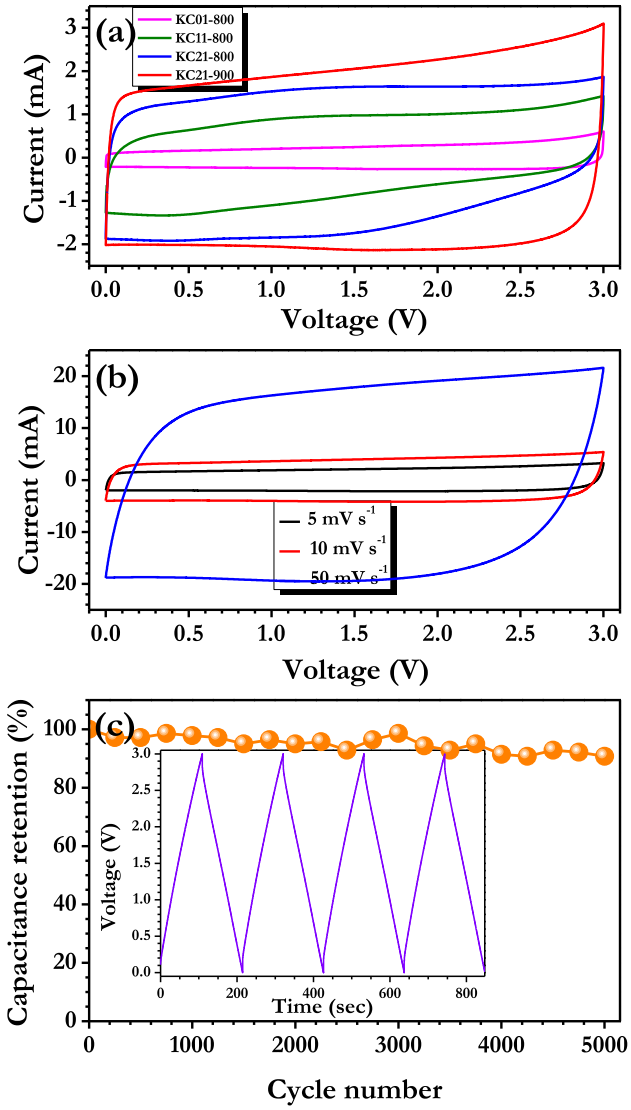

Fig. 4. (a) Comparison of CV traces of *Prosopis juliflora* derived carbons in symmetric supercapacitor configuration between 0 and 3 V at a scan rate of 5 mV s^{-1}. All the electrodes had 8 mg active mass loading, (b) CV traces of KC21-900 based symmetric supercapacitor at different scan rates between 0 and 3 V, and (c) Galvanostatic charge–discharge and cycling profile of KC21-900 at a current density of 1 A g^{-1}. (A color version of this figure can be viewed online.)

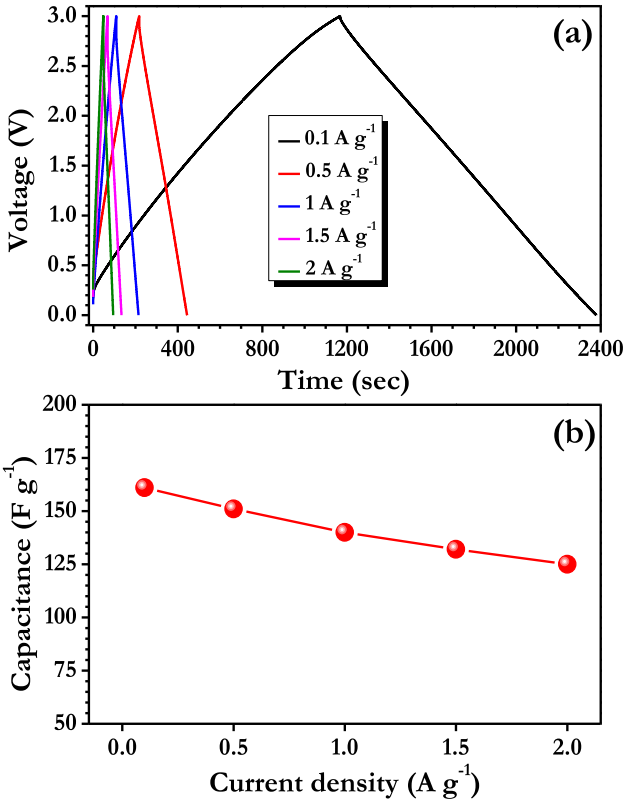

Fig. 5. (a) Galvanostatic charge–discharge profiles of a KC21-900 based symmetric supercapacitor at various current densities, (b) Plot of specific discharge capacitance *vs.* applied current density. (A color version of this figure can be viewed online.)

supported by CV studies (Fig. 6a). Similarly, the Li-insertion/extraction process of solid-state prepared LTO were well documented from in galvanostatic studies (Fig. S7b) and CV analysis (Fig. 6a). Thus, both types of electrode materials were exceptional in terms of their high specific capacity, high rate capability, and excellent cycling stability. This might be attributed to the intrinsic characteristics such as structure and morphology of the KC21-900 and LTO, which provided sufficient space for electrolyte diffusion and ensured high facile ion movement for Faradaic and non-Faradaic reactions. CV studies were performed for both electrodes and Li-HEC at a slow scan rate of 0.1 mV s^{-1} to understand the reaction kinetics and storage mechanism.

As shown in Fig. 6a, the KC21-900 electrode between 3 and 4.6 V *vs.* Li exhibit a perfect rectangular shape without any obvious redox peaks, which clearly reflects a characteristic EDLC behavior. A pair of well-defined sharp and intense anodic and cathodic peaks were observed for the case of LTO, which obviously suggests a perfect Li-insertion/extraction process with a two-phase reaction mechanism [8]. The observed voltage gap between redox peaks exhibited better kinetics and durability of the electrodes during electrochemical reactions. Unlike the sharp redox peaks observed in LTO, Li-HEC showed quasi-rectangular shaped curves within a 1–3 V range. This CV signature suggests the involvement of both Faradaic and non-Faradaic reactions in Li-HEC, and this is consistent with previous reports [11,38]. The CV curves of the Li-HEC recorded at different scan rates (5, 10, and 50 mV s^{-1}) are illustrated in Fig. 6b. When the sweep rates increased, the shapes of CV curves remained the same but more distortion was noted, indicating a fast Li-intercalation/de-intercalation along with a dominant supercapacitive behavior. This is very important for the high-rate operation of electrochemical power sources and is desirable from the EV and HEV point of view.

Galvanostatic charge–discharge measurements were conducted for Li-HEC at different current densities between 1 and 3 V and are given in Fig. 7 (and Fig. S8). Here, the applied current density was based on the total mass of both electrodes (13 mg). Compared to EDLC, no perfect linear curves were obtained for Li-HEC because of the redox behavior of the negative electrode resulting from the perfect Li-insertion/extraction process. In a typical charge process, Li-ion is intercalated in to LTO matrix and PF_6^- are adsorbed on the KC21-900 surface and eventually involves the double layer formation. Upon discharge, the aforesaid reaction was reversed [2].

Long cycle life or cycling stability is also an important parameter for Li-HEC to realize the practical use. In this regard, Li-HEC was cycled at a current density of 1 A g^{-1} and the obtained results are depicted in Fig. 8. Fig. 8a represents the cyclic retention and the coulombic efficiency of the Li-HEC cell as a function of cycle number. The cell retained ~76% of its initial value after 10, 000

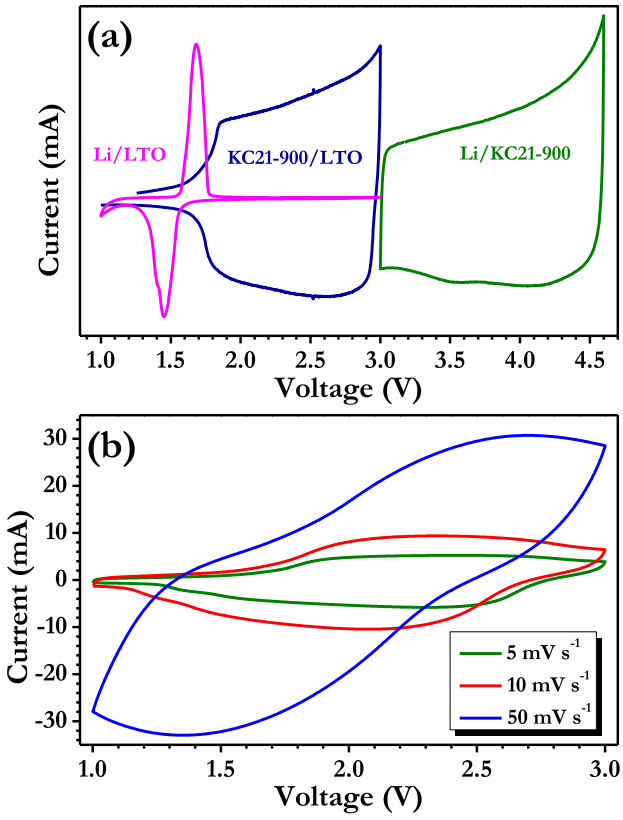

Fig. 6. (a) Comparison of CV traces at a slow scan rate of 0.1 mV s^{-1} for both KC21-900 and LTO in a single-electrode (half-cell) configuration between 3–4.6 and 1–3 V *vs.* Li, respectively. CV traces of KC21-900/LTO based Li-HEC is also given for comparison under the same scan rate between 1 and 3 V, (b) CV traces of KC21-900/LTO based Li-HEC at various scan rates. (A color version of this figure can be viewed online.)

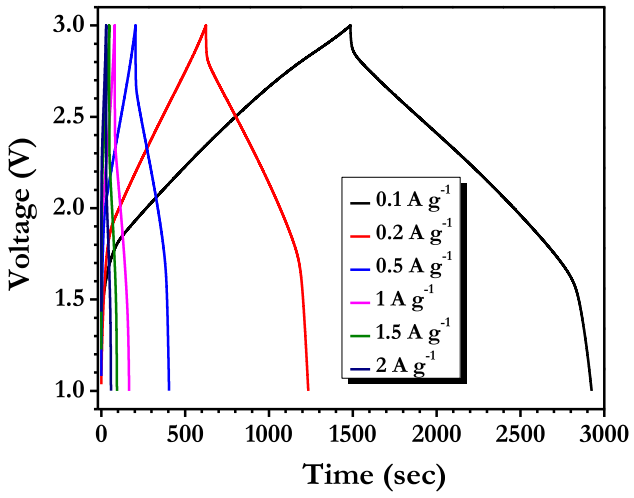

Fig. 7. Typical galvanostatic charge–discharge profiles of KC21-900/LTO based Li-HEC at different current densities. Here the current density is based on the total mass loading of the electrode. (A color version of this figure can be viewed online.)

cycles, showing that Li-HEC possesses an excellent stability upon prolonged cycling. We strongly believe that this outstanding electrochemical stability is mainly attributed to the tubular hollow carbon skeleton in KC21-900 with tailored micro and mesoporosities and the optimum amount of functional groups present in the carbonaceous electrode, apart from the high specific surface

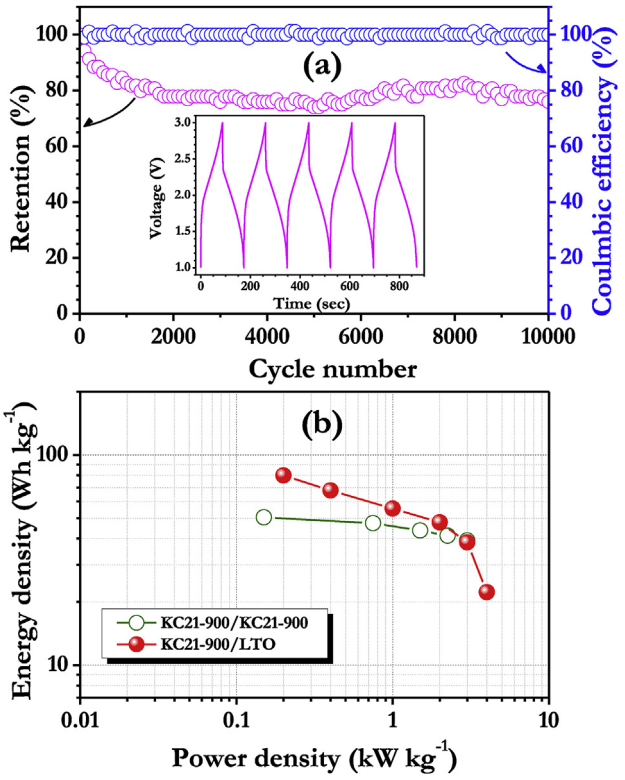

Fig. 8. (a) Plot of cyclic retention *vs.* cycle number and coulombic efficiency of KC21-900/LTO based Li-HEC at a current density of 1 A g^{-1}. Here, the current density is based on the total mass loading of the electrode. Inset: typical charge–discharge curves for the first five cycles, (b) Ragone plot of KC21-900 based symmetric and Li-HEC configuration. (A color version of this figure can be viewed online.)

area. Fig. 8b shows the Ragone plot of KC21-900 based Li-HEC with LTO and symmetric configuration. As mentioned earlier, both electrode masses were taken for the calculation of energy and power densities. Similarly, average potential (1.5 V for symmetric supercapacitor and 2 V for Li-HEC) were taken into account.

As expected, Li-HEC displayed the maximum energy density of ~80 W h kg^{-1} compared to ~50 W h kg^{-1} for KC21-900 based symmetric supercapacitor. Increases in current density *i.e.* power density tended to decrease energy density. At a high power density of 3 kW kg^{-1}, the energy density of KC21-900 based symmetric supercapacitors (~39 Wh kg^{-1}) was marginally higher than Li-HEC (~38 Wh kg^{-1}). This slightly inferior performance of the Li-HEC at high current rates was mainly due to the limited Li-ion kinetics in the insertion negative electrode, LTO. Nevertheless, this can be further improved by adopting either surface modification with carbon or composite formation and carbonaceous materials such as carbon nanotubes, carbon nanofibers, and graphene nanosheets [39]. On a side note, the observed values were much higher than that for activated graphene (~41 W h kg^{-1}) [10], shredded waste paper (~61 W h kg^{-1}) [12], metal organic framework derived carbon (~65 W h kg^{-1}) [38], and AC derived from coconut shell (~69 W h kg^{-1}) [11] based Li-HEC's. To the best of our knowledge, this is one of the highest values reported on Li-HEC, apart from the graphitic/hard carbon negative electrode [2].

The electrode kinetics and electrochemical performances of the Li-HEC cell are identified from Nyquist plots displayed in Fig. 9a. Each plot consists of a semicircle at high frequency region and a straight line at low frequency region. In the low-frequency region, the electrodes exhibit typical capacitive behavior due to the presence of nearly vertical tails, indicating facile Li-insertion/extraction

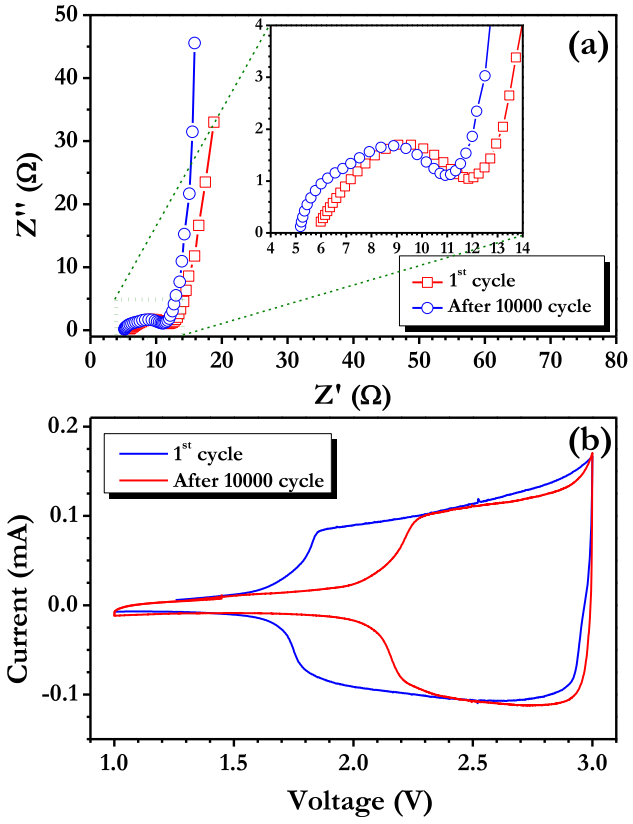

Fig. 9. (a) Electrochemical impedance spectra of KC21-900/LTO based Li-HEC recorded after the completion of the first and 10000 cycles and (b) CV traces of KC21-900/LTO based Li-HEC after the completion of the first and 10000 cycles. (A color version of this figure can be viewed online.)

[40]. A depressed semicircle was observed in the medium frequency region, which resulted from a parallel combination of the charge-transfer resistance (R_{ct}) caused by Li-insertion/extraction and a constant phase element. A small decrease in the solution resistance (R_s) from ~5.98 to ~5.19 Ω was noted after the prolonged cycling of 10,000 cycles. Similar to R_s, there was not much variation in the *Rct*, for example, the value of ~11.84 and ~10.93 Ω were observed for after 1st and 10000 cycles, respectively. This marginal decrease in the R_{ct} values certainly showed that the excellent stability and integrity of both electrodes towards the electrolyte solution. CV experiments were conducted for after 10,000 cycles at a lower scan rate and compared with first one (Fig. 9b). No apparent changes in the shape of the CV curves between first after 10000 cycles were noted except in an area under the curve. Reduction in the area was consistent with the long-term cycling profiles of Li-HEC. Overall, an excellent performance was noted for the *P. juliflora* wood derived carbon in both symmetric and hybrid configurations. This clearly showed the environmentally threatening tree wood could be easily transformed into potential electrodes for charge storage with low cost. Further studies are in progress to improve the cycleability and high power capability of the Li-HEC.

4. Conclusion

In this work, we successfully demonstrated the construction of Li-HEC using biomass derived carbon as supercapacitor component. *P. juliflora*-derived carbon treated at 900 °C with a 1:2 KOH ratio (KC21-900) has appealing properties. The morphological features and composition of the materials were confirmed by BET, SEM and XPS analysis. The KC21-900 based Li-HEC delivered a maximum energy density of ~80 W h kg^{-1} with 76% retention after 10000 cycles, offsetting the energy density of its symmetric configuration (~50 W h kg^{-1}). This reveals that an environmentally threatening invasive weed could be easily used as an electrode for energy storage devices such as EDLC and Li-HEC, eventually powering electric vehicles (EVs), hybrid EVs, and plug-in hybrid EVs in the future. Furthermore, this transformation of *P. juliflora* into an attractive energy storage material aids the “abolish *juliflora* movement” for environmental protection.

Acknowledgments

This work was supported by the International Collaborative Energy Technology R&D Program of the Korea Institute of Energy Technology Evaluation and Planning (KETEP), granted financial resource from the Ministry of Trade, Industry & Energy, Republic of Korea (No. 20128510010050).

Appendix A. Supplementary data

Supplementary data related to this article can be found at http://dx.doi.org/10.1016/j.carbon.2015.10.087.

References

[1] E.J. Cairns, P. Albertus, Batteries for electric and hybrid-electric vehicles, Annu. Rev. Chem. Biomol. Eng. 1 (1) (2010) 299–320.
[2] V. Aravindan, J. Gnanaraj, Y.-S. Lee, S. Madhavi, Insertion-type electrodes for nonaqueous Li-ion capacitors, Chem. Rev. 114 (23) (2014) 11619–11635.
[3] K. Naoi, S. Ishimoto, J-i Miyamoto, W. Naoi, Second generation 'nanohybrid supercapacitor': evolution of capacitive energy storage devices, Energy Environ. Sci. 5 (11) (2012) 9363–9373.
[4] K. Naoi, Y. Nagano, Li-ion-based Hybrid Supercapacitors in Organic Medium. Supercapacitors, Wiley-VCH Verlag GmbH & Co. KGaA, Weinheim, Germany, 2013, pp. 239–256.
[5] I. Plitz, A. DuPasquier, F. Badway, J. Gural, N. Pereira, A. Gmitter, et al., The design of alternative nonaqueous high power chemistries, Appl. Phys. A Mater. Sci. Process. 82 (4) (2006) 615–626.
[6] A.D. Pasquier, I. Plitz, J. Gural, F. Badway, G.G. Amatucci, Power-ion battery: bridging the gap between Li-ion and supercapacitor chemistries, J. Power Sources 136 (1) (2004) 160–170.
[7] G.G. Amatucci, F. Badway, A. Du Pasquier, T. Zheng, An asymmetric hybrid nonaqueous energy storage cell, J. Electrochem. Soc. 148 (8) (2001). A930–A9.
[8] V. Aravindan, Y.S. Lee, S. Madhavi, Research progress on negative electrodes for practical Li-ion batteries: beyond carbonaceous anodes, Adv. Energy Mater. 5 (2015) 1402225.
[9] R. Gokhale, V. Aravindan, P. Yadav, S. Jain, D. Phase, S. Madhavi, et al., Oligomer-salt derived 3D, heavily nitrogen doped, porous carbon for Li-ion hybrid electrochemical capacitors application, Carbon 80 (0) (2014) 462–471.
[10] M.D. Stoller, S. Murali, N. Quarles, Y. Zhu, J.R. Potts, X. Zhu, et al., Activated graphene as a cathode material for Li-ion hybrid supercapacitors, Phys. Chem. Chem. Phys. 14 (10) (2012) 3388–3391.
[11] A. Jain, V. Aravindan, S. Jayaraman, P.S. Kumar, R. Balasubramanian, S. Ramakrishna, et al., Activated carbons derived from coconut shells as high energy density cathode material for Li-ion capacitors, Sci. Rep. 3 (2013). Art 3002.
[12] D. Puthusseri, V. Aravindan, B. Anothumakkool, S. Kurungot, S. Madhavi, S. Ogale, From waste paper basket to solid state and Li-HEC ultracapacitor Electrodes: a value added journey for shredded office paper, Small 10 (21) (2014) 4395–4402.
[13] D. Puthusseri, V. Aravindan, S. Madhavi, S. Ogale, Improving the energy density of Li-ion capacitors using polymer-derived porous carbons as cathode, Electrochim. Acta 130 (0) (2014) 766–770.
[14] H. Kim, K.-Y. Park, M.-Y. Cho, M.-H. Kim, J. Hong, S.-K. Jung, et al., High-performance hybrid supercapacitor based on graphene-wrapped $Li_4Ti_5O_{12}$ and activated carbon, ChemElectroChem. 1 (1) (2014) 125–130.
[15] A.G. Pandolfo, A.F. Hollenkamp, Carbon properties and their role in supercapacitors, J. Power Sources 157 (1) (2006) 11–27.
[16] S. Chhatre, V. Aravindan, D. Puthusseri, A. Banerjee, S. Madhavi, P.P. Wadgaonkar, et al., High surface area porous carbon for ultracapacitor application by pyrolysis of polystyrene containing pendant carboxylic acid groups prepared via click chemistry, Mater. Today Commun. 4 (2015) 166–175.
[17] K. Karthikeyan, S. Amaresh, S.N. Lee, X. Sun, V. Aravindan, Y.-G. Lee, et al., Construction of high-energy-density supercapacitors from pine-cone-derived high-surface-area carbons, ChemSusChem. 7 (5) (2014) 1435–1442.

[18] J. Yan, Q. Wang, T. Wei, Z. Fan, Recent advances in design and fabrication of electrochemical supercapacitors with high energy densities, Adv. Energy Mater. 4 (4) (2014) 1300816.
[19] L. Wei, G. Yushin, Nanostructured activated carbons from natural precursors for electrical double layer capacitors, Nano Energy 1 (4) (2012) 552–565.
[20] N. Arun, A. Jain, V. Aravindan, S. Jayaraman, W. Chui Ling, M.P. Srinivasan, et al., Nanostructured spinel $LiNi_{0.5}Mn_{1.5}O_4$ as new insertion anode for advanced Li-ion capacitors with high power capability, Nano Energy 12 (0) (2015) 69–75.
[21] J.H. Park, O.O. Park, Hybrid electrochemical capacitors based on polyaniline and activated carbon electrodes, J. Power Sources 111 (1) (2002) 185–190.
[22] A.C. Ferrari, D.M. Basko, Raman spectroscopy as a versatile tool for studying the properties of graphene, Nat. Nanotechnol. 8 (4) (2013) 235–246.
[23] A.C. Ferrari, J. Robertson, Interpretation of Raman spectra of disordered and amorphous carbon, Phys. Rev. B 61 (20) (2000) 14095–14107.
[24] V. Aravindan, W. Chuiling, M.V. Reddy, G.V.S. Rao, B.V.R. Chowdari, S. Madhavi, Carbon coated nano-$LiTi_2(PO_4)_3$ electrodes for non-aqueous hybrid supercapacitors, Phys. Chem. Chem. Phys. 14 (16) (2012) 5808–5814.
[25] M. Saravanan, P. Sennu, M. Ganesan, S. Ambalavanan, Multi-walled carbon nanotubes percolation network enhanced the performance of negative electrode for lead-acid battery, J. Electrochem. Soc. 160 (1) (2013). A70–A6.
[26] J. Wang, S. Kaskel, KOH activation of carbon-based materials for energy storage, J. Mater. Chem. 22 (45) (2012) 23710–23725.
[27] A. Elmouwahidi, Z. Zapata-Benabithe, F. Carrasco-Marín, C. Moreno-Castilla, Activated carbons from KOH-activation of argan (Argania spinosa) seed shells as supercapacitor electrodes, Bioresour. Technol. 111 (0) (2012) 185–190.
[28] Q. Wang, L. Jiao, H. Du, Y. Si, Y. Wang, H. Yuan, Co_3S_4 hollow nanospheres grown on graphene as advanced electrode materials for supercapacitors, J. Mater. Chem. 22 (40) (2012) 21387–21391.
[29] G. Wang, J. Zhang, S. Kuang, S. Liu, S. Zhuo, The production of cobalt sulfide/graphene composite for use as a low-cost counter-electrode material in dye-sensitized solar cells, J. Power Sources 269 (0) (2014) 473–478.
[30] N. Dwivedi, R.J. Yeo, N. Satyanarayana, S. Kundu, S. Tripathy, C.S. Bhatia, Understanding the role of nitrogen in plasma-assisted surface modification of magnetic recording media with and without ultrathin carbon overcoats, Sci. Rep. 5 (2015) 7772.
[31] Z. Yang, M. Xu, Y. Liu, F. He, F. Gao, Y. Su, et al., Nitrogen-doped, carbon-rich, highly photoluminescent carbon dots from ammonium citrate, Nanoscale 6 (3) (2014) 1890–1895.
[32] J. Baltrusaitis, C.R. Usher, V.H. Grassian, Reactions of sulfur dioxide on calcium carbonate single crystal and particle surfaces at the adsorbed water carbonate interface, Phys. Chem. Chem. Phys. 9 (23) (2007) 3011–3024.
[33] B. Kumar, M. Asadi, D. Pisasale, S. Sinha-Ray, B.A. Rosen, R. Haasch, et al., Renewable and metal-free carbon nanofibre catalysts for carbon dioxide reduction, Nat. Commun. 4 (2013) 2819.
[34] J.H. Lee, W.H. Shin, M.-H. Ryou, J.K. Jin, J. Kim, J.W. Choi, Functionalized graphene for high performance lithium ion capacitors, ChemSusChem. 5 (12) (2012) 2328–2333.
[35] P. Simon, P.-L. Taberna, F. Béguin, Electrical Double-layer Capacitors and Carbons for EDLCs. Supercapacitors, Wiley-VCH Verlag GmbH & Co. KGaA, Weinheim, Germany, 2013, pp. 131–165.
[36] T. Brousse, D. Bélanger, D. Guay, Asymmetric and Hybrid Devices in Aqueous Electrolytes. Supercapacitors, Wiley-VCH Verlag GmbH & Co. KGaA, Weinheim, Germany, 2013, pp. 257–288.
[37] V. Khomenko, E. Raymundo-Pinero, F. Beguin, Optimisation of an asymmetric manganese oxide/activated carbon capacitor working at 2 V in aqueous medium, J. Power Sources 153 (1) (2006) 183–190.
[38] A. Banerjee, K.K. Upadhyay, D. Puthusseri, V. Aravindan, S. Madhavi, S. Ogale, MOF-derived crumpled-sheet-assembled perforated carbon cuboids as highly effective cathode active materials for ultra-high energy density Li-ion hybrid electrochemical capacitors (Li-HECs), Nanoscale 6 (8) (2014) 4387–4394.
[39] K. Naoi, W. Naoi, S. Aoyagi, J-i Miyamoto, T. Kamino, New Generation "Nanohybrid Supercapacitor", Accounts Chem. Res. 46 (5) (2013) 1075–1083.
[40] V. Aravindan, K. Karthikeyan, K.S. Kang, W.S. Yoon, W.S. Kim, Y.S. Lee, Influence of carbon towards improved lithium storage properties of Li_2MnSiO_4 cathodes, J. Mater. Chem. 21 (8) (2011) 2470–2475.